Extraction of short wind wave spectra from stereo images of the sea surface

2011 Meas. Sci. Technol. 22 015504

(http://iopscience.iop.org/0957-0233/22/1/015504)

Meas. Sci. Technol. **22** (2011) 015504 (9pp) doi:10.1088/0957-0233/22/1/015504

Extraction of short wind wave spectra from stereo images of the sea surface

Mariya V Kosnik and Vladimir A Dulov

Remote Sensing Department, Marine Hydrophysical Institute, Kapitanskaya str. 2, Sevastopol 99011, Ukraine

E-mail: mvkosnik@gmail.com

Received 7 June 2010, in final form 8 November 2010
Published 13 December 2010
Online at stacks.iop.org/MST/22/015504

Abstract
A combined method is proposed to estimate the spectra of short wind waves. The spectra extracted from stereo pairs of the sea surface are used for the absolute calibration of the slope spectra obtained with Fourier-processing of the same high-resolution photo images. The calibration extends significantly the range of scales of stereo-retrieved waves toward the shortest ones. The method was adjusted and validated *in situ*. Algorithms and their experimental validation are presented, covering a range of wavelengths from 30 cm up to 6 mm, for different wind speeds. Spectral shapes and levels are consistent with earlier experimental data and models.

Keywords: short wind wave spectra, stereo photography, image processing, field study

1. Introduction

Field measurements of the sea surface roughness of horizontal scales 1 mm to 1 m are of great interest for both scientific and applied marine problems. Capillary and short gravity wavelets, wavebreaking and microbreaking, and other coherent structures result in complex geometrical and dynamical properties of the sea surface [1–3]. This surface geometry determines the signal retrieved from most satellite imaging systems, in particular synthetic aperture radars and other active or passive microwave instruments. Air–sea exchange processes are also largely controlled by this short-scale roughness of the sea surface [4, 5]. The aerodynamic surface drag has a particularly strong influence on the atmospheric boundary layer, and defines the momentum flux from atmosphere to the ocean circulation [6]. Laboratory measurements do not easily address this issue because the properties of the natural atmospheric boundary layer are difficult to reproduce in tank facilities. Therefore, empirical information on the small-scale sea roughness remains sparse despite its importance for remote sensing, climate studies and environmental monitoring [7].

The two-dimensional (2D) spatial spectrum of the surface elevation is a common statistical measure of sea roughness. Usual measurements of sea elevations at fixed points by means of water-immersed sensors encounter fundamental difficulty in estimating frequency spectra at small scales because of Doppler shifting due to advection of short waves by orbital velocities of longer waves [8, 9]. A number of remote sensing methods were proposed to obtain 2D spatial spectra, including scanning lidar and radar systems [10, 11]. However, passive optical methods using photographic sea images are most convenient for practical application in field conditions. There are two main approaches in obtaining 2D spectra with the aid of sea image recording:

(i) spectrum estimation following the stereoscopic recovery of the surface;
(ii) direct Fourier-processing of a brightness pattern on the image.

A stereo-based method has a long history of applications to the estimation of the wave spectrum (see e.g. [12–14], among others). It was extended to use video recordings of the sea [15] and improved to measure the finest structures on water surface in laboratory conditions [16]. The central problem of the method is to find and localize pairs of corresponding points which are images of the same object in two snapshots of the water surface made from different views. Once the matching points are found, the surface topography can be recovered using standard procedures [15, 16]. In the laboratory, objects can be artificially introduced on the water surface to facilitate the matching of points. For instance, the water surface was stained by white dye in the experiment of Tsubaki and Fujita [16]. In field conditions, the only suitable objects are brightness variations induced by surface waves. Whitecaps on the breaking wave crests are particular objects but their infrequent occurrence cannot provide enough corresponding points even during a storm [17]. In practice, the recovery of the surface topography of waves of a given scale requires the detection of brightness variations due to smaller scale waves. Moreover, along the wavelength of the stereo-resolved wave, many such brightness variations are to be identified. This fact is the principal constraint for the spatial resolution of the stereo-based method. In particular, the shortest waves cannot be recovered because there are no smaller objects on the sea surface.

The 2D-spectrum estimation with direct Fourier-processing of a brightness pattern on a single snapshot was widely used in the earlier studies of the sea surface roughness [18–20]. Spatial resolution of this method is limited only by camera angle resolution and can be improved so as to resolve shortest objects on the sea surface. However, the method allows only relative measurements. Additional measurements of sea surface heights or slopes have to be made during photographing to normalize the spectrum and obtain an absolute-calibrated spectral estimation. This important drawback alongside with restrictions to uniform sky illuminance conditions limits the adaptation of the method in field studies. Note that a variant of this approach was proposed in [21], where the sea surface is photographed from the aircraft and the sun glitter geometry described by Cox and Munk [22] is utilized for an absolute calibration. However, this methodology is applicable to the spectrum estimation of long waves only.

It appears clearly desirable to develop an approach combining the advantages of both methods. In fact, the same stereo pair of snapshots can be processed with the two methods, and the stereo-based data can be used for the absolute calibration of the high-resolution brightness spectrum. This paper is aimed at describing such an attempt. Details of both methods and the way to combine them are discussed below. A dedicated field experiment was performed to develop the details of the data processing. The validity and merits of the approach are demonstrated in this paper.

2. Procedure

2.1. Experiment

The experiment was carried out in October–November 2009 on the Black Sea Research Platform of Marine Hydrophysical Institute, Sevastopol. The Platform is located 500 m from the coast in a water depth of about 30 m. The stereo system consisted of two synchronized cameras SONY DSC-R1 with 72 mm focal length and angle of view $17^\circ \times 11^\circ$, rigidly mounted at a height of 4.5 m above the mean sea level (see figure 1). The distance between the two cameras was 1.5 m, and the view angle was 30° relative to the horizon providing a maximum area of picture intersection. The pictures were taken in raw format and converted to 16-bit uncompressed TIFF format with the resolution 3888 by 2592 pixels. The resulting spatial resolution on the sea surface was of the order of 1 mm per pixel with an area covered of 3×4 m^2. The exact camera position and intrinsic camera parameters were obtained from a separate calibration step with a chessboard pattern, using standard procedures [23]. Camera synchronization was provided with the LANC Shepherd device (see the description of the device, for example, at www.berezin.com/3d/Lanc/user.html)[1] connected through the LANC port. The synchronizer button was pressed manually every 5–10 s, giving the impulse to the camcorders of both cameras to take snapshots simultaneously with accuracy better than 0.1 ms. Exposure time of both cameras was set small enough (typically 1 ms) to register millimeter capillary waves moving with wavespeeds up to 1 m s^{-1} (this value corresponds to the orbital velocities of dominant waves in Black Sea storm conditions). We used the green color channel of the cameras for further processing. Every experimental series consisted of 80–100 lossless format pair pictures being taken during 15–20 min. Depending on sky illumination, sea state, etc, 30–80 of these pairs were found good enough to process. During the time of one experiment series wind and sea surface conditions could not change significantly and enough data for statistical treatment could be collected. String resistant wave gauge recordings were running simultaneously providing information about the gravity wave spectrum.

Figure 1. View of the stereoscopic equipment used for the experiment.

In this paper we present the results of data processing for several series covering different wind–wave situations. The summary of experimental conditions is presented in table 1.

2.2. Stereo-based approach

2.2.1. Stereo photo processing. The method of sea surface reconstruction from stereo pair of photographs is widely described in the literature [15, 16, 23]. For calculating spatial coordinates, we used a standard approach based on epipolar geometry and the pinhole camera model with distortion correction.

[1] Berezin Stereo Photography Products, 21686 Abedul, Mission Viejo, CA 92691, USA (www.berezin.com exists since 2009).

Table 1. Environmental and acquisition parameters during the experiment.

Run no	Date	Local time	Wind speed at 10 m level (m s^{-1})	Wind direction	Swell direction	Number of stereo pairs processed
1	6 Oct.	16:10–16:35	5	N (offshore)	SSW	47
2	7 Oct.	10:15–10:40	10	E	–	72
3	19 Oct.	16:00–16:20	13–17	E	–	67
4	26 Oct.	13:10–13:20	13	E	–	27
5	28 Oct.	14:50–15:10	7	N (offshore)	W	76

The principal difficulty of short wave photograph processing in field conditions consists in matching of corresponding pixels on stereo pairs because sharply defined texture does not exist on the whole sea surface. In contrast to gravity waves photographing where short waves serve as markers, in our case they are the subject of investigation themselves. The only objects forming texture on their surface are capillary ripples that do not appear everywhere and in all weather conditions. So the search for homologous points needs maximum efforts and accuracy. To realize it, we follow the next steps.

2.2.2. Homologous points search algorithm.

(i) We search corresponding points roughly by means of a correlation procedure on eight times diminished pairs of images. These points are utilized to find with the least-squares method a spatial cubic transformation of one high-resolution photo onto another. Thus, we exclude the problem of possible slightly different scales and orientations of corresponding objects on pairs of images. Furthermore, after the transformation the object on a surface has approximately the same pixel coordinates both on the right and on the left images. It constricts essentially the region for further correlation analysis and therefore the computational time while seeking precise corresponding points. The cubic transformation is chosen instead of the projective one because in our case it fits better—the sea is not far enough from the cameras and long waves with scales of the order of observation area do not allow us to consider the surface as a plane. Thus, some corrections for this effect are needed and they are included in the polynomial transform. A stereo pair of photos before and after transformation of the left image is shown in figure 2. One can see that the scale and pixel position of large structures become similar on pictures (*b*) and (*c*) (this is better seen on the borders).

(ii) Another feature making correlation analysis more effective is a Fourier filter applied to both the images. All spatial frequencies corresponding to scales more than 1/30 of image size are zeroed in two-dimensional Fourier space, and an inverse FFT is performed. In such a way only texture with no brightness trends remains.

(iii) In order to decrease the number of false correlations, several criteria are used. First, the analysis is not performed in regions with low texture, namely the normalized pixel intensity $[\max(I) - \min(I)]/\mathrm{mean}(I)$ defined in a 30×30 pixel window, should exceed 0.5, where I is the intensity of the pixels. This parameter is not influenced by smooth brightness gradients in the picture because these have been filtered out in the previous step. Second, matching homologous points, defined by the maximum of correlation in the pair of images, are validated only where this correlation coefficient is greater than 0.5. Third, after this correlation analysis left and right pictures are permuted, and homologous points are searched in the same way for every obtained point. If these new points do not agree closely with initial points, they are excluded from further consideration.

The coordinates of the matching points are then transformed back onto initial (non-distorted) photos and triangulation is made. More than 10 000 points are usually obtained to recover surface topography from one pair of photos. A final filtering of false points is implemented after triangulation. Namely points with elevation above mean sea surface exceeding four standard deviations are removed. This removal is performed iteratively, with five to ten iterations. At every iteration the mean sea level is approximated by a third-order polynomial surface using the remaining points.

2.2.3. Assessment of stereo-based sea roughness recovery. To demonstrate the work of the stereo-based sea surface reconstruction method, we present several parts of retrieved surfaces with starting wave breaking events. Fragments of pictures with corresponding topography and several cross-sections in the wave propagation direction are plotted in figure 3. The pictures show breaking waves with wavelength close to 1 m. The wave steepness, ak, is about 0.4, which is in agreement with laboratory observations and numerical modeling of breaking waves [24].

Likely the best quantitative way to validate the stereo-based method is to compare stereoscopic data spectra with wave staff gauge recordings running simultaneously. Sea surface reconstructed for every stereo pair was divided into 10–15 overlapping parts and two-dimensional wavenumber Fourier expansion was calculated for each of them. The spectrum for the whole series is obtained by ensemble averaging of all these instantaneous spectra. An omnidirectional spectrum results from integrating this spectrum over the wave direction. The problem of its comparison with wave gauge data is the transfer from frequency space to wavenumber space where we obtain stereo data statistics. As a rough approach we accept a classical dispersion relation for gravity waves disregarding Doppler and nonlinear effects. Thus, the conversion of the frequency spectrum to the wavenumber spectrum reads

$$S(k(f)) = S(f)/|\mathrm{d}k/\mathrm{d}f| = gS(f)/(8\pi^2 f)$$

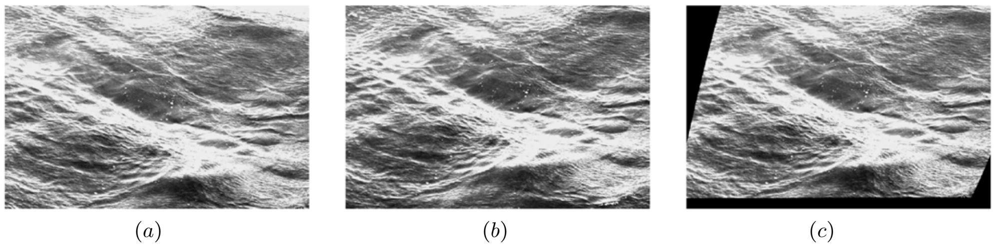

Figure 2. First step of the image processing: stereo pair. Left photo (*a*), right photo (*b*) and left photo after cubic transformation (*c*).

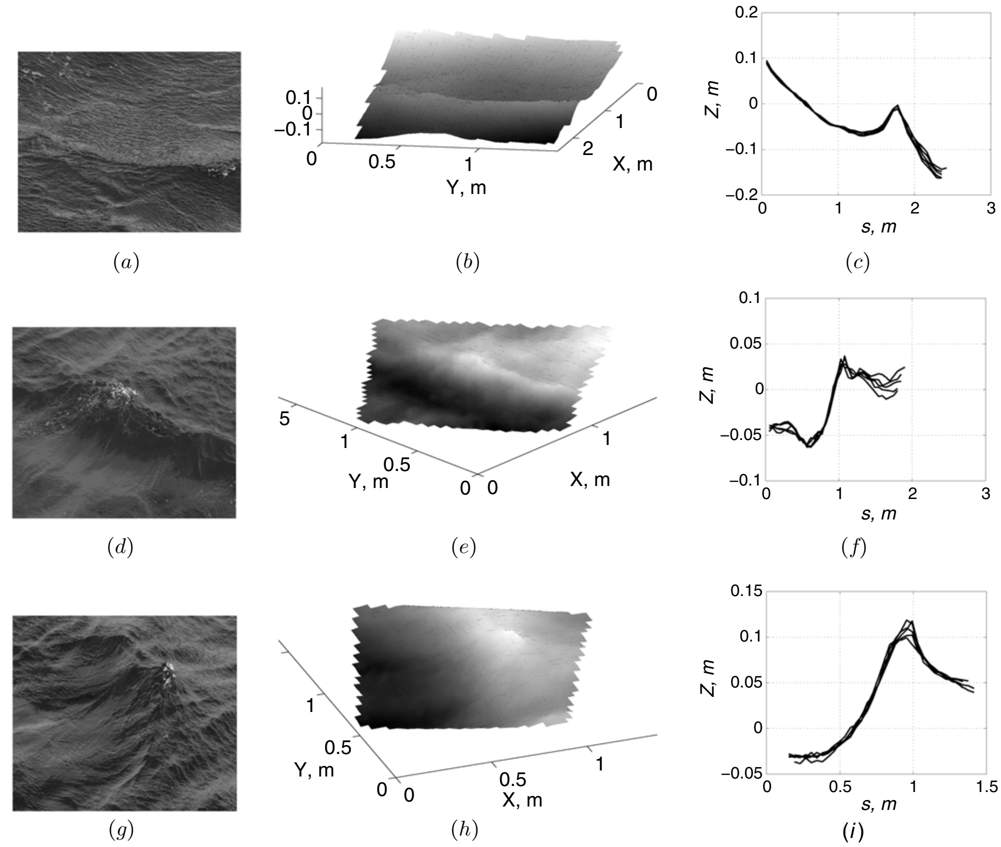

Figure 3. Reconstructed starting wave-breaking events. Fragments of the picture (left), reconstructed surfaces (middle) and cross-sections in the wave propagation direction (right).

where g is the gravity acceleration. We found that the energy levels at the edges of stereoscopic and wavegauge data are in agreement for all five series. Examples of the comparison of wavenumber spectra derived from photographs and wavegauge frequency spectra are shown in figure 4.

2.3. *Brightness-based approach*

2.3.1. Basic model. Complicated spatial variability of the sea surface radiance results from non-uniformity of sky-radiance distribution, upwelled radiation from beneath the surface, and modulations by surface waves due to angle-dependent Fresnel reflection, multiple reflections and shading [20, 22]. As shown by Cox and Munk (see their figures 4–6 in [22]) in the range of view angles from 45° up to 70° relative to the vertical, the sky radiance with the single reflection mechanism forms mainly the observable brightness pattern of the sea surface. For this case a small part of the sea surface perturbed by waves can be considered as a plane with local slopes $\zeta_x = \partial\zeta/\partial x$ and $\zeta_y = \partial\zeta/\partial y$, where ζ is the surface elevation. Supposing the wave slopes to be small, the brightness at the fixed point of the photograph can be given by an expansion

$$I = C_0 + C_x\zeta_x + C_y\zeta_y + C_{xx}\zeta_x^2 + C_{xy}\zeta_x\zeta_y + C_{yy}\zeta_y^2 + \cdots \tag{1}$$

where the coefficients depend on point coordinates due to sky-radiance non-uniformity and angle dependence of Fresnel coefficients. Considering a small enough area of the sea surface image, we will neglect this dependence.

Thus, to the first order in small slopes we obtain a relation between Fourier transforms of photo brightness and sea elevations,

$$I_{\mathrm{k}} = \mathrm{i}(k_x C_x + k_y C_y)\zeta_k \tag{2}$$

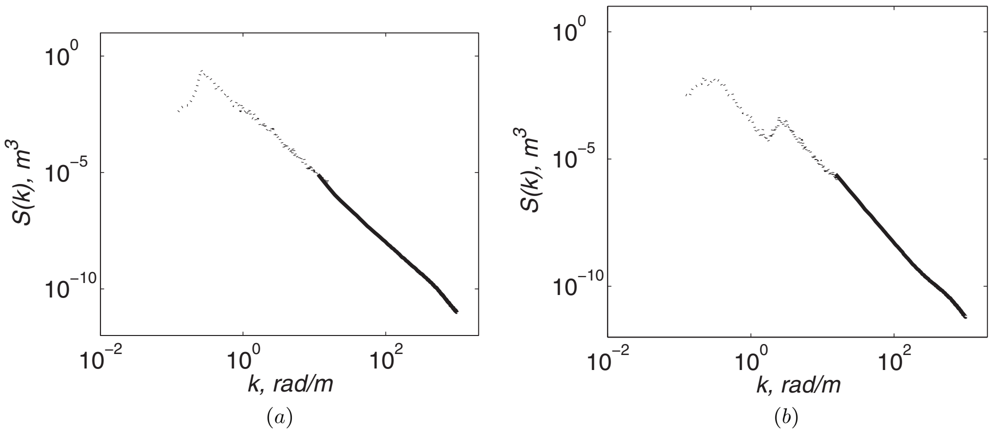

Figure 4. Comparison of wave spectra obtained from staff gauge and stereo photo recordings for runs 3(*a*) and 5(*b*). The dashed and solid lines correspond to wave staff and photo data, respectively. The upper part of the solid line is obtained with the stereo-based method.

where $\mathbf{k} = (k_x, k_y)$ is the wavenumber vector and i is the imaginary unit. From here the elevation spectrum $S(\mathrm{k}) = \langle \zeta_k \zeta_{-k} \rangle$ can be estimated as

$$S = J/(k_x C_x + k_y C_y)^2 \tag{3}$$

where $J(\mathbf{k}) = \langle I_k I_{-k} \rangle$ is the brightness spectrum, and averaging is performed over the series of pictures and/or various parts of each picture.

Based on this idea the 2D-spectra of the sea surface were evaluated in a number of studies ([18–21] and others). Monaldo and Kasevich [20] evaluated the coefficients in (1) with a model and considered the errors of the method. However, the constants C_x and C_y are commonly unknown, so the method is difficult to use in field conditions.

As follows from (2) and (3) the method fails in the vicinity of the line $k_x C_x + k_y C_y = 0$ on the $\mathbf{k}$ plane. In this case the omitted quadratic terms of equation (1) have to be accounted for. That is, the brightness contrast for the wavenumber $\mathbf{k}$ in this area no longer corresponds to the slope component of the same wavenumber.

In the polar coordinates $\mathbf{k} = (k\cos\varphi, k\sin\varphi)$, equation (3) reads

$$S_2(\mathbf{k}) = \frac{J(\mathbf{k})}{C\cos^2(\varphi - \varphi_0)} \tag{4}$$

where $S_2 = k^2 S$ is the slope spectrum of the sea surface, $C = C_x^2 + C_y^2$, $\tan\varphi_0 = C_y/C_x$. As follows from here if we find the value of C and φ_0 through some calibration procedure for long waves, then it can be used in estimating the shorter wave spectrum because the values of C and φ_0 are independent of the wavenumber k.

Furthermore, an algorithm for obtaining these constants with the help of stereoscopic data will be developed and the gravity-capillary spectra will be inferred according to equation (4). Since the method is applicable for the spectral components whose directions are inside the interval $|\varphi - \varphi_0| < \Delta$, the values of φ_0 and Δ will also be determined in the processing of photographs.

2.3.2. Brightness spectra and MTF correction. Image smoothing because of optical imperfections, image registering system, and image transformations during processing causes contrast damping at small scales. An account of that is of principal significance for our study. In estimating the brightness spectra, an optical transfer function, OTF(k), is commonly applied to remove this effect (see, e.g., [25]). By definition, the OTF is the Fourier transform of a point spread function, $D(x, y)$, where $D(x, y, x_0, y_0)$ is the response to impulse brightness distribution localized at the point $\delta(x - x_0, y - y_0) = \delta(x - x_0)\delta(y - y_0)$, and (x, y) are orthogonal coordinates at the object plane. Then the apparent brightness pattern, $A(x, y)$, is a convolution of D and the real brightness field

$$A(x, y) = \int D(x, y, x_0, y_0) I(x_0, y_0)\, \mathrm{d}x_0\, \mathrm{d}y_0. \tag{5}$$

For the linear shift-invariant systems, $D(x, y, x_0, y_0) = D(x - x_0, y - y_0)$, Fourier transforms are simply related [25]:

$$A_k = \mathrm{OTF}(\mathbf{k}) I_k. \tag{6}$$

In our case $A = P[I]$, where P is the projective transformation for perspective view that cannot be treated as linear with respect to the coordinates (x, y). Therefore, the point spread function is not shift-invariant for our entire pictures. However, we can apply equation (6) locally for different small fragments of the picture, using a local OTF. In line with this idea, the following steps were made to estimate the brightness spectra.

(i) The point spread function D_0 for the top view was defined in laboratory conditions. We use the screen divided by a straight line into uniform black and white halves. Photographing of the screen was made at the distance corresponding to the field working range. 1D point spread functions were obtained by differentiation of a step-like brightness pattern on the photos. We found that the point spread functions for horizontal and vertical directions at the photo are equal. Further we use the point spread function in the form $D_0 = d(x)d(y)$ with the shape of d obtained experimentally.

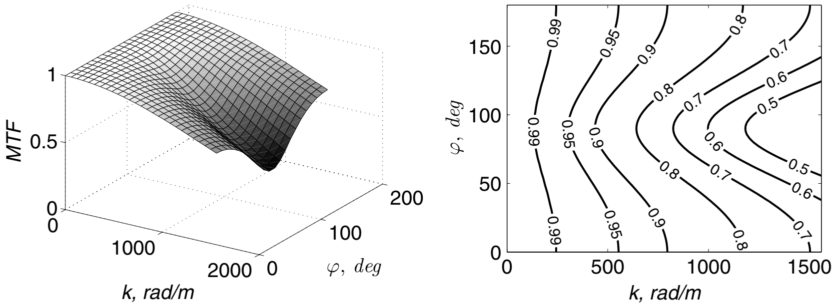

(*a*) (*b*)

Figure 5. Two-dimensional modulation transfer function. Spatial view (*a*) and isolines (*b*).

(ii) After selecting the image fragment for Fourier expansion, D_0 was projected onto the horizontal plane corresponding to the sea surface to obtain the local point spread function $D = P^{-1}[D_0]$, where P is the projective transformation known for this fragment after stereo processing. Then D was Fourier-transformed to obtain the local OTF. The shape of MTF = |OTF| (called the modulation transfer function [25]) for the central part of the photo is shown in polar coordinates in figure 5. The anisotropy of the MTF implies stretching of the image pixels in the forward direction when the photo is projected on the sea surface. As clearly seen in part (*b*) of the figure, this effect has to be accounted for at wavenumbers greater than 500 rad m^{-1}.

(iii) The selected image fragment was also projected at the horizontal sea surface, and the fixed regular grid was placed into the area. The fixed grid at the sea surface provides the fixed grid at the wavenumber plane that simplifies subsequent averaging of the spectra. The grid points were transformed back into the image plane to find brightness values for them. The brightness values were defined with linear interpolation at the regular image grid. After that the Fourier transformation was performed using 2D Hann windowing (see e.g. [26]). Finally the values of Fourier transforms were corrected according to (6) with the use of local MTF.

Further the estimations of $I_k I_{-k}$ were averaged over all the fragments and over all the photos of each run to obtain the brightness spectra $J(\mathbf{k})$. Note that we had to exclude the photos contaminated by foam due to whitecapping. The total numbers of processed pair of images are shown in table 1.

2.3.3. Recovery of wave slope spectra. Applicability of equation (4) is determined by the validity of the linear approach and negligible spatial variability of C that are expressed by equation (2). We can examine this equation having the estimations of brightness and sea surface elevation spectra for overlapping **k**-domains over the same area of the sea surface. The measure of correspondence is given by the coherence function γ and the phase shift function Ψ [25, 26]:

$$\gamma = |\langle I_k \zeta_{-k}\rangle| / \sqrt{J(\mathbf{k})S(\mathbf{k})}, \qquad \Psi = \mathrm{angle}(\langle I_k \zeta_{-k}\rangle).$$

According to equation (2) the phase shift must be close to $\pi/2$ at the **k**-domain where the coherence function is close to unity. These functions are shown in figure 6 for run 4 as an example. We can see that linear dependence between Fourier components of brightness and sea elevations occurs actually within central areas of the plots. For smaller k, reliable spectral estimations are obviously difficult to obtain because their spatial scale corresponds to the scale of considered sea surface area. For higher k the stereoscopic approach must fail as expected. The restrictions of the angular range are also predicted in section 2.3.1 (see equation (4)). Note that MTF-correction of brightness spectra does not affect the functions γ.

Table 2. Threshold φ_1, φ_2.

Run number	φ_1 (deg)	φ_2 (deg)
1	25	155
2	0	130
3	25	155
4	25	155
5	25	155

Then we consider the rectangle in the **k**-domain

$$k_1 < k < k_2, \qquad \varphi_1 < \varphi < \varphi_2, \tag{7}$$

which is definitely located within the threshold contour $\gamma = 0.5$. We have chosen k-borders as $k_1 = 30$ rad m^{-1} and $k_2 = 50$ rad m^{-1} for all the runs and φ-borders as listed in table 2. Further we define

$$\varphi_0 = (\varphi_1 + \varphi_2)/2, \qquad \Delta = |\varphi_1 - \varphi_2|/2$$

to recover higher wavenumber spectra only in the range $|\varphi - \varphi_0| < \Delta$.

From brightness spectral density, we calculate the function $F(\mathbf{k}) = J(\mathbf{k})/\cos^2(\varphi - \varphi_0)$. Then we can find the value of C in the least-squares sense according to (4) with the use of F and S_2 data from the coherence rectangle (7). Figure 7 shows examples of the ratio J/S_2 normalized by C and averaged over the interval $k_1 < k < k_2$. A plot of $\cos^2(\varphi - \varphi_0)$ is also depicted. The agreement with equation (4) is evident. Figure 8 shows the ratios F/S_2. These functions were normalized by C and averaged over the interval $\varphi_1 < \varphi < \varphi_2$ for each of the runs. The ratios are actually close to unity and independent of k in the range of coherence from 30 rad m^{-1} up to 50 rad m^{-1}. Thus, the experiment shows that the linear approach (2)–(4) is valid.

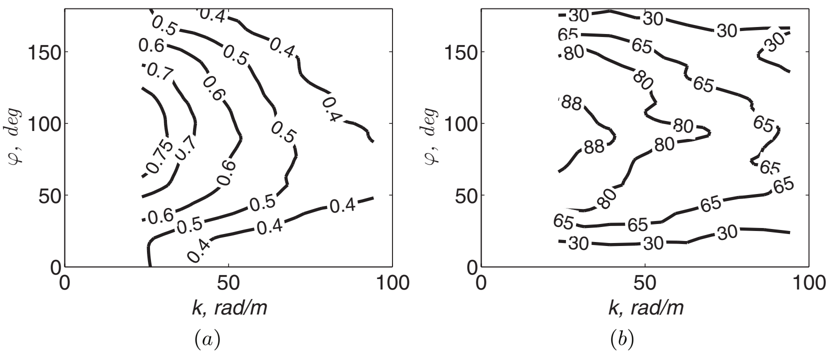

Figure 6. Interrelation between wave elevation and brightness: spatial brightness–elevation coherence (*a*) and phase between brightness and elevation Fourier transforms (*b*).

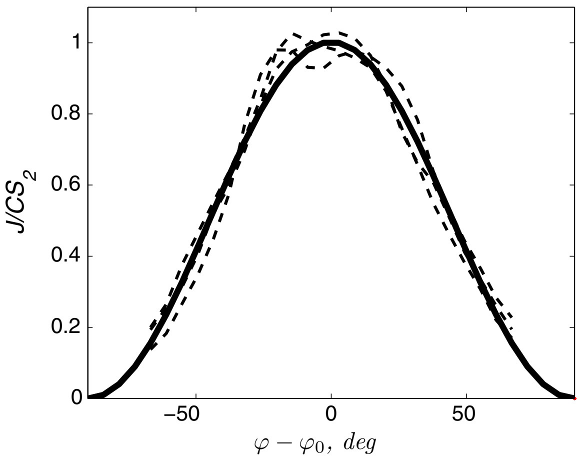

Figure 7. Proof of linear approach validity. Examples of the brightness to slope spectrum ratio integrated over the wavenumber and normalized by C (dashed lines) and the $\cos^2(\varphi - \varphi_0)$ function (solid line).

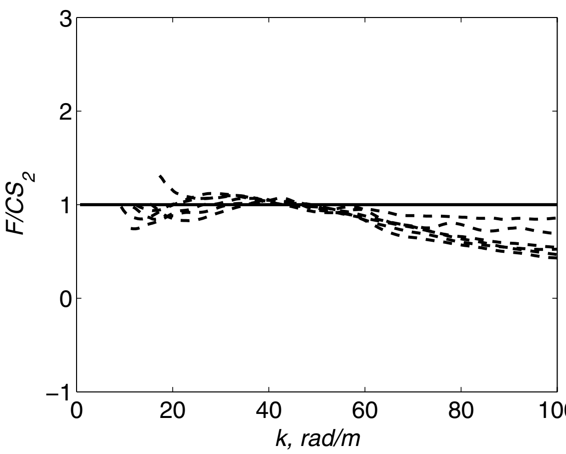

Figure 8. Brightness to slope spectrum ratio divided by $C\cos^2(\varphi - \varphi_0)$ and averaged over the wave direction for runs 1–5 (dashed lines). The ratio is close to unity (solid line) in the coherence zone (30 rad m^{-1} $< k <$ 50 rad m^{-1}).

Finally, we can determine the absolute-calibrated slope spectrum for all wavenumbers in the angular range $\varphi_1 < \varphi < \varphi_2$ as F/C.

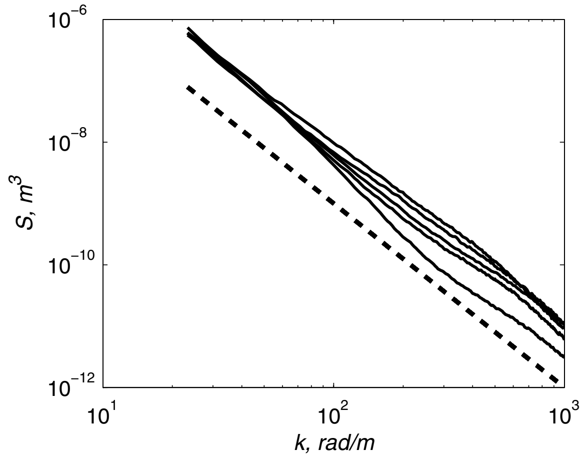

Figure 9. Elevation spectra and the k^{-3} curve.

3. Discussion of results

In figure 4 examples of omnidirectional spectra retrieved with the combined method from photography series are shown. The upper parts of the spectra for $k < 50$ rad m^{-1} were obtained with the stereoscopic method. The stereoscopic and brightness spectra coincide in the parts corresponding to 30 rad m^{-1} $< k <$ 50 rad m^{-1}. For higher wavenumbers the spectra were obtained with brightness processing. In computing the omnidirectional spectra by integration over φ the unknown spectral parts for $|\varphi - \varphi_0| > \Delta$ were linear interpolated. A more detailed view of all the short wave spectra is shown in figure 9. The spectrum slope of k^{-3} found in the earlier experiment of Banner *et al* [14] is also drawn in the figure. We can see only marginal agreement. Better agreement exists for lower wavenumbers $k < 50$ rad m^{-1} where the spectra collapse. For higher wavenumbers we can clearly see that the spectrum level grows gradually with the increase of wind speed. This effect is well known in ocean radar technology. Scatterometers' wind speed determination above the ocean is based on its application.

Combining the spectra which were estimated with the staff wave gauge and photography, we obtain the whole omnidirectional slope spectrum $S_2 = k^2 S$. Then the mean

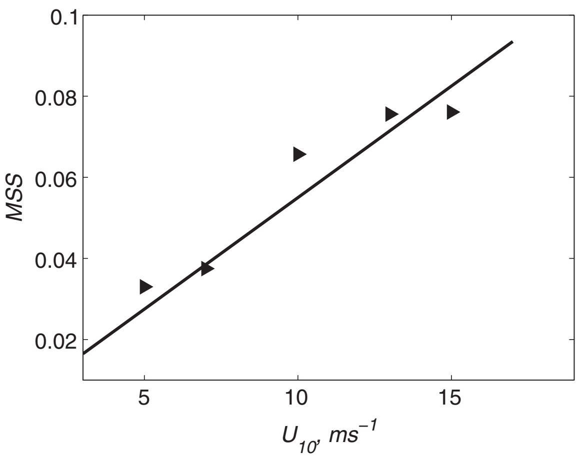

Figure 10. Mean square slope variance depending on wind speed. Runs 1–5 (triangles). Solid line—[22].

square slope variance, MSS $= \int S_2(k)\,\mathrm{d}k$, was computed by integration over the joint wavenumber range. The MSS values are plotted against the wind speed in figure 10. As can be seen, these data are in satisfactory agreement with the classical Cox and Munk dependence [22].

Figure 11 outlines the angular dependence of the spectra. Note that photo registering can resolve the propagation direction of a wave with uncertainty of 180°, so the angular spectra obtained are related to the actual ones as $S(\varphi) = (S_{\mathrm{act}}(\varphi) + S_{\mathrm{act}}(\varphi + \pi))/2$. Further we use Phillips' saturation function, $B(\mathbf{k}) = k^4 S$, for a more detailed presentation of spectra. The saturation spectra B were integrated over the ranges 20 rad m^{-1} $< k <$ 100 rad m^{-1}, 100 rad m^{-1} $< k <$ 500 rad m^{-1}, 500 rad m^{-1} $< k <$ 900 rad m^{-1} and normalized to put their maxima at unity. The unknown spectral parts for $|\varphi - \varphi_0| > \Delta$ give rise to gaps near 0° and 180°. We can clearly see anisotropy of angular dependence. Maxima of spectra correspond approximately to the wind direction indicated by the vertical dashed line.

In figure 12 empirical information on the omnidirectional B is summarized, and all our data are also presented. Kudryavtsev *et al* [27] developed a physical model for the short wave spectra. This model reproduces results of laboratory

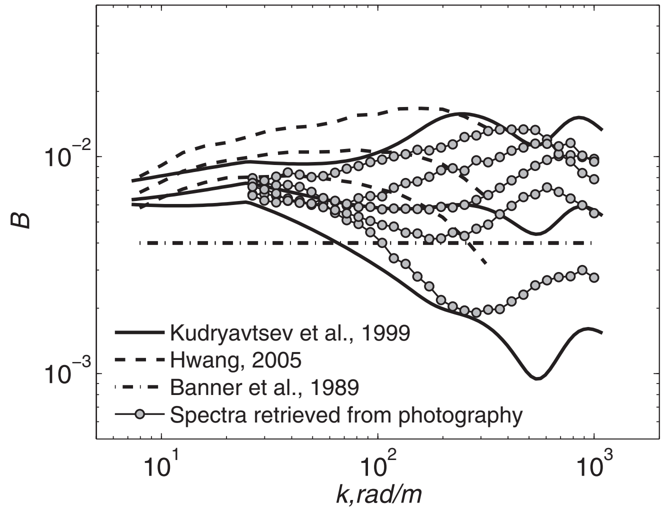

Figure 12. Saturation spectrum for runs 1–5. A comparison with other models (see the text).

measurements [2, 28, 29]. In the figure, the spectra [27] are drawn for wind speeds of 6, 10 and 17 m s^{-1}. The constant level according to Banner *et al* [14] and the parameterization of Hwang [30] based on field study for wind speeds of 6, 10 and 17 m s^{-1} are also shown. All our spectra lie within the limits of scatter of known data. In the capillary and capillary-gravity ranges, the spectral level grows gradually following the increase of wind speed, and in the gravity range the spectra converge. The prominent feature of our spectra is a dip in the area of phase speed minimum that becomes filled in if the wind speed grows. The dip was earlier observed in laboratory study [2], and was discussed in [27, 31, 32]. Dulov and Kosnik [32] have shown that the dip is caused by three-wave interactions in the capillary-gravity range. Thus we can conclude that the combined approach to spectra extraction from photographs gives quite realistic results.

4. Conclusion

A combined method of short wind wave spectrum estimation in field conditions has been proposed and demonstrated. This

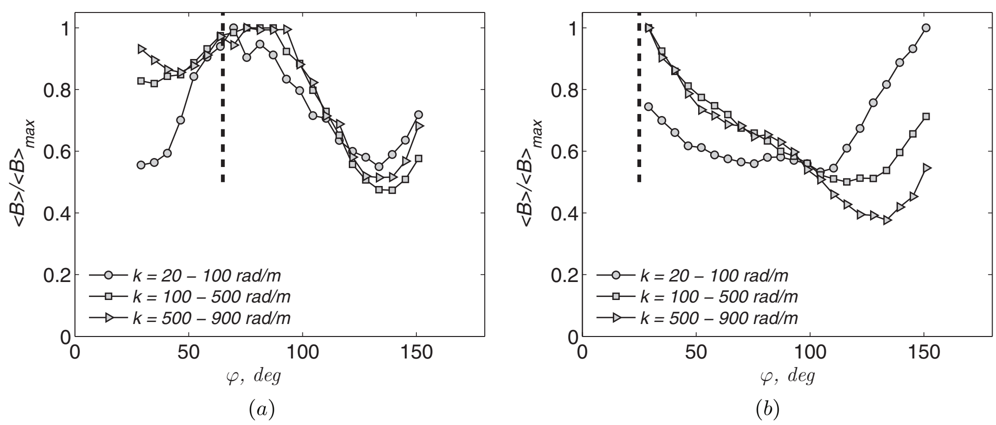

Figure 11. Angular shape of the curvature spectrum. The mean saturation function normalized on its maximum value in three wavenumber ranges. Run 4(*a*) and run 1(*b*). The dashed line corresponds to the approximate wind direction.

method combines two techniques: stereo photography and brightness processing. The brightness-based method gives information about the shortest waves, down to the picture resolution, that cannot be detected in the stereo-based method while the stereo-based method serves to obtain absolute calibration for the brightness spectrum and a robust estimate of longer waves. This method was tested at different wind velocities in field conditions. Particularly, it has been shown that the mean square slope variance given by our method is consistent with estimates by Cox and Munk based on sun glitter analysis, and the omnidirectional saturation spectra are consistent with known empirical information and theoretical results.

Work with this method is clearly possible not only from the rigid platform but also from moving bearers, say ships, providing the exposure time diminished enough to prevent blurring. Developments of this method are possible in two directions. The use of the camera with improved spatial resolution at the sea surface will allow us to study the shortest capillary waves the spectra of which remain unclear. An application of video recording will give the possibility of studing the 3D spatio-temporal spectra of short wind waves.

Acknowledgments

The authors are very grateful to Vladimir Kudryavtsev (Nansen International Environmental and Remote Sensing Center, St Petersburg) and Fabrice Ardhuin (IFREMER, Brest) for the deep discussions and useful remarks, and also to V Malinovsky, V Smolov, Yu Yurovsky, A Korinenko and A Mironov (Marine Hydrophysical Institute) for their assistance throughout the field experiments. This work was supported by National Academy of Sciences of Ukraine under the contract no 12/09 and Fundamental Researches State Fund of Ukraine under the contract F28/435-2009.

References

[1] Dias F and Khariv C 1999 Nonlinear gravity and capillary-gravity waves *Annu. Rev. Fluid Mech.* **31** 301–46

[2] Zhang X 1995 Capillary-gravity and capillary waves generated in a wind wave tank: observations and theories *J. Fluid Mech.* **289** 51–82

[3] Ebuchi N, Kawamura H and Toba Y 1987 Fine structure of laboratory wind-wave surfaces studied using an optical method *Bound.-Layer Meteorol.* **39** 133–51

[4] Donelan M and Wanninkhov R 2002 Gas-transfer at water surfaces—concepts and issues *Gas-Transfer at Water Surfaces (Geophysical Monograph* vol 127) ed M Donelan (Washington, DC: American Geophysical Union) pp 1–10

[5] Garratt J R *et al* 1992 *The Atmospheric Boundary Layer (Cambridge Atmospheric and Space Science Series)* (Cambridge: Cambridge University Press) p 316

[6] Kudryavtsev V N and Makin V K 2002 Coupled dynamics of short waves and the airflow over long surface waves *J. Geophys. Res.* **107** 3209

[7] Munk W 2009 An inconvenient sea truth: spread, steepness, and skewness of surface slopes *Annu. Rev. Mar. Sci.* **1** 377–415

[8] Kitaigordskii S A, Krasitskii V P and Zaslavskii M M 1975 On Phillips' theory of equilibrium range in the spectra of wind-generated gravity waves *J. Phys. Oceanogr.* **5** 410–20

[9] Hwang P A 2006 Doppler frequency shift in ocean wave measurements: frequency downshift of a fixed spectral wave number component by advection of wave orbital velocity *J. Geophys. Res.* **111** 6033

[10] Hwang P A, Atakturk S, Sletten A and Trizna D B 1996 A study of the wavenumber spectra of short water waves in the ocean *J. Phys. Oceanogr.* **26** 1266–85

[11] Krogstad H, Lehner S, Monbaliu J, Wyatt L, Hauser D and Kahma K 2005 *Measuring and Analysing the Directional Spectrum of Ocean Waves* ed J R Garratt (Brussels: COST)

[12] Pierson W 1962 The directional spectrum of a wind generated sea as determined from data obtained by the stereo wave observation project *Coll. Eng, N.Y.U. Met. Pap.* **2**

[13] Holthuijsen L H 1983 Observations of the directional distribution of ocean-wave energy in fetch-limited conditions *J. Phys. Oceanogr.* **13** 191–207

[14] Banner M L, Trinder J C and Jones I S F 1989 Wavenumber spectra of short gravity waves *J. Fluid Mech.* **198** 321–44

[15] Benetazzo A 2006 Measurements of short water waves using stereo matched image sequences *Coast. Eng.* **53** 1013–32

[16] Tsubaki R and Fujita I 2005 Stereoscopic measurement of a fluctuating free surface with discontinuities *Meas. Sci. Technol.* **16** 1894–902

[17] Mironov A S and Dulov V A 2008 Detection of wave breaking using sea surface video records *Meas. Sci. Technol.* **19** 015405

[18] Stilwell D Jr 1969 Directional energy spectra of the sea from photographs *J. Geophys. Res.* **74** 1974

[19] Sugimori Y 1975 A study of application of the holographic method to the determination of the directional spectrum of ocean waves *Deep-Sea Res.* **22** 335–50

[20] Monaldo F M and Kasevich R S 1981 Daylight imagery of ocean surface waves for wave spectra *J. Phys. Oceanogr.* **11** 272–83

[21] Grodsky S, Kudryavtsev V, Bol'shakov A and Burdjugov V 1990 Two-dimensional surface elevation spectra from airphoto data *Izv. Atmos. Ocean. Phys.* **26** 652–8

[22] Cox C and Munk W 1954 Measurement of the roughness of the sea surface from photographs of the sun's glitter *J. Opt. Soc. Am.* **44** 838–50

[23] Bouguet J Y 2004 Camera Calibration Toolbox for Matlab. Personal website: www.vision.caltech.edu/bouguetj/calib_doc

[24] Babanin A 2009 Breaking of ocean surface waves *Acta Phys. Slovaka* **59** 305–535

[25] Jähne B 2002 *Digital Image Processing* 5th edn (Berlin: Springer)

[26] Piersol A G and Bendat J S 1986 *Analysis and Measurement Procedures* (New York: Wiley)

[27] Kudryavtsev V N, Makin V K and Chapron B 1999 Coupled sea surface–atmosphere model 2. Spectrum of short wind waves *J. Geophys. Res.* **104** 7625–40

[28] Jähne B and Riemer K S 1990 Two-dimensional wave number spectra of small-scale water surface waves *J. Geophys. Res.* **95** 11531–46

[29] Hara T, Bock E J and Donelan M 1997 Frequency-wavenumber spectrum of wind-generated gravity-capillary waves *J. Geophys. Res.* **102** 1061–72

[30] Hwang P A 2005 Wave number spectrum and mean square slope of intermediate-scale ocean surface waves *J. Geophys. Res. (Oceans)* **110** 10029

[31] Elfouhaily T, Chapron B, Katsaros K and Vandemark D 1997 A unified directional spectrum for long and short wind-driven waves *J. Geophys. Res.* **102** 15781–96

[32] Dulov V A and Kosnik M V 2009 Effects of three-wave interactions in the gravity-capillary range of wind waves *Izv. Atmos. Ocean. Phys.* **45** 408–19